Dalton Transactions

PAPER

View Article Online
View Journal

Cite this: DOI: 10.1039/c9dt01783f

Metal-catalyst-free access to multiwalled carbon nanotubes/silica nanocomposites (MWCNT/SiO_2) from a single-source precursor

Gabriela Mera, *[a] Peter Kroll, *[b] Ilia Ponomarev, [b] Jiewei Chen,[c] Koji Morita,[d] Moritz Liesegang,[a] Emanuel Ionescu [a] and Alexandra Navrotsky [c]

The present study introduces a facile single-source precursor preparative access to bamboo-like multiwalled carbon nanotubes (MWCNTs) highly dispersed within a mesoporous silica-rich matrix. The metal-free single-source precursor was synthesized *via* a one-pot sol–gel process using tetramethyl orthosilicate (TMOS) and 4,4′-dihydroxybiphenyl (DHBP) and converted subsequently *via* pyrolysis under an argon atmosphere into MWCNT/silica nanocomposites. The *in situ* segregation of the highly defective bamboo-like MWCNTs was carefully investigated and has been shown to occur within the mesopores of the silica-rich matrix at relatively low temperatures and without the use of a metal catalyst. The experimental results have been supported by extensive computational simulations, which correlate the molecular architecture of the single-source precursor with the structural features of the carbon phase segregating from the silica matrix. Furthermore, the role of hydrogen in the stability of the prepared nanocomposites as well as in the high-temperature evolution and morphology of the segregated MWCNTs has been discussed based on vibrational spectroscopy, calorimetric studies and empirical potential calculations. The results obtained within the present study may allow for designing highly-defined nanocarbon-containing composites with tailored structural features and property profiles.

Received 29th April 2019,
Accepted 9th June 2019

DOI: 10.1039/c9dt01783f

rsc.li/dalton

Introduction

Carbon nanotubes (CNTs) as important one-dimensional nanomaterials with outstanding electrical, thermal and mechanical properties have great potential for various applications in electronics, energy, composites, drug delivery, nanoimaging *etc*. Since Iijima's report in 1991 on the synthesis of multiwalled carbon nanotubes (MWCNTs),[2] various methods have been explored in order to access this type of 1D nanocarbon. Significant scientific interest was focused especially on CNTs exhibiting exotic structures such as bamboo and fish-bone morphologies.[3–5] Bamboo-like MWCNTs, firstly reported by Saito and Yoshikawa,[6] consist of graphene shells with a "stacked cone" morphology and consequently possess significantly higher concentrations of structural defects as compared to hollow MWCNTs. These defects are formed due to the incorporation of heteroatoms into the graphene shells. Since the mechanical and electronic properties of CNTs strongly depend on their chirality, diameter, defect structure, *etc*., such nanotubes have entered the spotlight of nano-science.[7] Having a structure composed of separated hollow compartments and bamboo knots, bamboo-like nanotubes found applications in several fields, such as sensors, adsorbents, catalysts, hydrogen-storage, lithium-ion battery electrode materials and silicon-based technology.[8]

Typically, CNTs are produced *via* vapor–liquid–solid (VLS) processes catalyzed by 3d valence transition metals (Fe, Co and Ni), noble metals such as Au, Ag and Cu, as well as main group metals such as Pb and In.[9–17] Unfortunately, the catalysts remain in the CNTs as undesired impurities after synthesis. Catalyst poisoning, as reported in several publications,[18,19] constitutes the major drawback of this route due to the ability of the metals to decompose hydrocarbons and to induce the post-rearrangements of the CNTs. The catalysts can be removed post-synthesis through aggressive chemical treatments; however, their purification usually does not fully eliminate metal particles and introduces defects into the carbon nanotubes.

[a]*Technische Universität Darmstadt, Institut für Materialwissenschaft, Otto-Berndt-Str. 3, D-64287 Darmstadt, Germany. E-mail: mera@materials.tu-darmstadt.de*
[b]*The University of Texas at Arlington, Department of Chemistry and Biochemistry, 700 Planetarium Place, Arlington, TX 76019, USA*
[c]*National Institute for Materials Science, Research Center for Functional Materials, Tsukuba, Ibaraki 305-0047, Japan*
[d]*University of California at Davis, Peter A. Rock Thermochemistry Laboratory and NEAT ORU, Davis, CA 95616, USA*

Recently, non-metallic catalysts for the synthesis of nanotubes such as SiC,[20] Ge,[21] MgO,[22] Al_2O_3,[23] ZrO_2,[24] magnesium borates[25,26] and SiO_2 [27–30] were reported. Templated CNTs can be grown in porous alumina without catalyst particles, as published by Schneider *et al.*[31] Particularly oxides were demonstrated to be capable of graphitizing carbon.[32]

Metal-free carbon nanotubes are desirable materials for wide potential applications.[33] The use of SiO_2 as a catalytically active species is particularly attractive for integration into Si based technology and its use as a carbon nanotube catalyst has been reported by various groups.[27–29,34] A key question regarding the use of SiO_2 as a graphitization catalyst relates to the possible transient generation of SiC forms during the process.[30,35]

Herein we are reporting for the first time on the catalyst-free *in situ* generation of MWCNTs within a silica-rich matrix during the thermal decomposition of a carbon-rich polysiloxane. Typically, preceramic polysiloxanes and polysilsesquioxanes may be used as suitable precursors for silicon oxycarbides.[36–40] Depending on their substitution patterns, the preceramic polymers may deliver the so-called carbon-rich polymer-derived silicon oxycarbides (*i.e.*, ceramics containing more than 20 wt% excess carbon, also denoted as free carbon),[41] which represent a special class of unique materials with the free carbon phase conferring a multitude of interesting functional properties like electro-optical, magnetic, sensorics, Li-ion permeability and storage as well as high adsorption/desorption for several gases.[36–40] The free carbon in silicon oxycarbides not only makes these materials "smart" but also strongly influences their thermal stability against crystallization and decomposition, their ceramic yield as well as the sizes of composing nanodomains. Thus, they possess a much higher stability against crystallization than their low-carbon containing analogues.

Amorphous silicon oxycarbide polymer-derived ceramics (PDCs), synthesized from polysiloxanes, contain carbon and silica-rich nanodomains, the latter with extensive substitution of carbon for oxygen, linking Si-centered SiO_xC_{4-x} tetrahedra.[37,39] Calorimetric studies demonstrated these PDCs to be thermodynamically more stable than a mixture of SiO_2, C, and SiC.[38] Nevertheless, the thermodynamic stability of these materials depends to a high extent on the microstructural features of the free carbon phase, as well as on the presence and concentration of hydrogen in their composition.[38]

Many characterization methods have several restrictions with respect to the investigation of amorphous ceramic systems. The rearrangement reaction of the carbon phase as a function of temperature is a very complex process. Therefore, a significant emphasis was placed on computational methods to elucidate the structure of as well to understand the organization of free carbon during the thermal decomposition process. Modeling and simulations of amorphous materials thus can greatly enhance the experimental resolution and provide new insights into the structure of disordered materials.

Results and discussion

Synthesis approach

Polymer-derived silicon oxycarbide (SiOC) ceramics are materials which can be obtained by the thermal treatment of polysiloxanes under an inert atmosphere.[39] Even if SiOC PDCs are X-ray amorphous materials, they are exhibiting unique structural features such as reduced mass fractal dimension and nano-heterogeneity (mass fractal dimensions of 2.4–2.5 and nanodomains of 1–3 nm in size), which significantly affect and/or dictate their properties and behavior. The short-range structure of the silicon oxycarbide glass is composed of a network of corner-shared silicon-centered tetrahedra incorporating both Si–C and Si–O but no C–O bonds (SiO_xC_{4-x} tetrahedra). The network is distinct from a mixture of separate, intergrown silicon carbide and silicon oxide nanophases and exhibits the full range of mixed bonded SiO_xC_{4-x} tetrahedra (*i.e.*, SiO_4, SiO_3C, SiO_2C_2, $SiOC_3$, and SiC_4). A different microstructural organization was reported for the silicon oxycarbide ceramics synthesized under CO_2 flow (Fig. 1a).[1,42,43] In this case, no mixed SiO_xC_{4-x} units were found, their structure being composed exclusively of SiO_2 and free C nanodomains.

The aim of the present study was to produce novel amorphous silicon oxycarbide ceramics with non-mixed bonds by simple thermal decomposition of polysiloxanes under an inert atmosphere. In order to achieve that, the molecular structure of the precursor was designed in such a way in order to comprise exclusively Si–O bondings. The carbon-containing groups should be bonded to silicon through C–O–Si bridges (*i.e.*, no Si–C direct bondings) (Fig. 1). This approach can assess the design of microstructures with controlled carbon phases in a porous silica matrix.

The synthesis of single-source precursors was accomplished *via* a one-pot sol–gel process using tetramethyl orthosilicate (TMOS), 4,4′-dihydroxybiphenyl (DHBP) and ethanol as co-solvents (Fig. 2). The white xerogel obtained after hydrolysis and condensation of the mixture in the presence of water was pyrolyzed at 900 °C under an argon atmosphere to deliver amorphous Si–O–C powders which were subsequently hot pressed at 1600 °C and 30 MPa in argon to produce dense monolithic specimens.

X-ray diffraction. The ceramic samples obtained *via* pyrolysis at 900 °C are X-ray amorphous (Fig. 3). The amorphous halo at

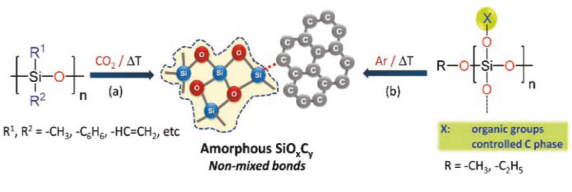

Fig. 1 Synthesis approach toward non-mixed bonded SiO_xC_y ceramics (*i.e.*, C/SiO_2 nanocomposites) *via* pyrolysis of polysiloxanes under a CO_2 atmosphere[1] (a) or *via* thermal decomposition of orthosilicate-based sol–gel systems containing large, aromatic organic substituents (b). The difference in the novel approach (b) consists of using precursors containing no Si–C bonding in the structure, with silicon being bonded only to oxygen.

Fig. 2 Sol–gel synthesis of orthosilicate-based single-source precursors containing large, aromatic substituents (a); their ceramization at 900 °C and uniaxial hot pressing at 1600 °C under an Ar atmosphere to produce monolithic ceramic samples (b).

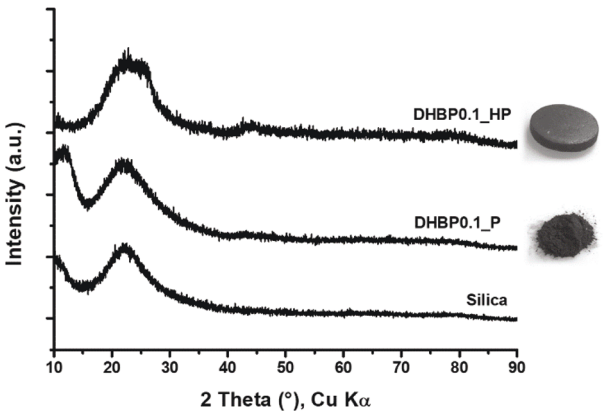

Fig. 3 X-ray diffraction of the powder sample synthesized at 900 °C (DHBP0.1_P) of the ceramic pellet produced at 1600 °C (DHBP0.1_HP) as compared to silica obtained at 900 °C.

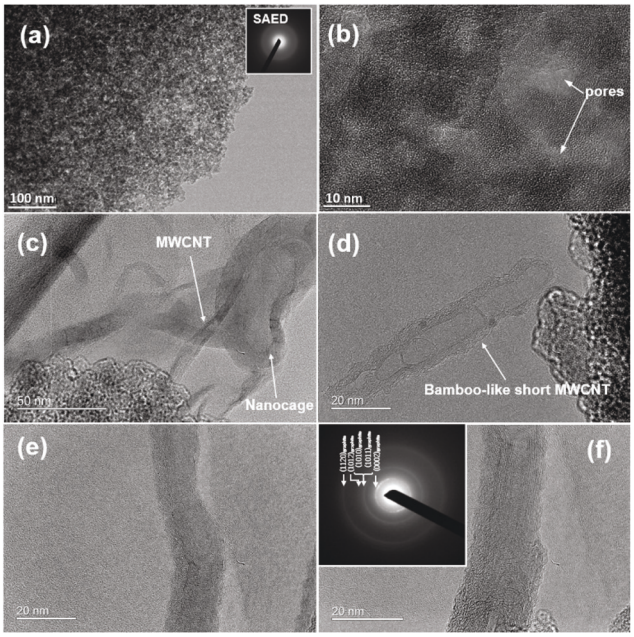

Fig. 4 Transmission electron microscopy image of DHBP0.1_P revealing (a) and (b) the microporous structure, (c) the presence of long defective MWCNTs as well as bean-like carbon nanocages; (d) short bamboo-like carbon nanotubes; (e) and (f) defective long bamboo-like MWCNTs where scrolls coexist within a tube.

2-theta values of ~22–25° corresponds to an overlapping of amorphous silica and carbon. Surprisingly, even after the hot-pressing step at 1600 °C, the ceramic nanocomposite presents only amorphous halos in XRD, corresponding to nanosilica and nanocarbon. Rather unusual for SiOC PDCs, no carbothermal reaction ($SiO_2 + C \rightarrow$ ß-SiC + 2 CO) was registered. The carbothermal reaction of silica generally occurs in PDCs *via* two reactions: (i) $SiO_2(s) + C(s) = SiO(g) + CO(g)$ and (ii) $SiO(g) + 2C(s) = SiC(s) + CO(g)$.

High-resolution TEM (HRTEM). High-resolution TEM (HRTEM) is a powerful method in order to locally investigate the nanostructure of polymer-derived ceramics, especially with respect to the nature and organization of the nanocarbon phase. Even if the PDCs are X-ray amorphous at low temperatures (T < 1400 °C), they are typically heterogeneous at the nanoscale, by various TEM studies.[38,44,45]

No major contrast variation was observed for the sample annealed at 900 °C (Fig. 4), indicating its amorphous nature. This information is indicated also by the SAED inset in Fig. 4f showing a diffuse elastically scattered ring pattern, typical of amorphous samples. A high resolution TEM micrograph (Fig. 4b) reveals the mesoporous nature of the sample with pores of ~6–10 nm in size. The mesopores are embedded in an amorphous matrix consisting of round silica nanoparticles of 5–7 nm in size. Surprisingly, as shown in Fig. 4c, the free carbon phase is represented by long and short multiwalled carbon nanotubes (MWCNTs) (length >300 nm) as well as a minor phase of bean-like graphene nanocages (100 nm long and ~30 nm broad).

The presence of short defective bamboo-like MWCNTs (~6 walls) is observed in Fig. 4d. The external wall of the tube seems to contain several point-like defects and/or functional groups on the surface. The inner chambers of the bamboo-like tube are separated by two graphene walls. The curvature of the compartment layers is directed to the tip.

The measured length of CNTs is in between 80 nm and 300 nm or more. Representative micrographs of long MWCNTs are shown in Fig. 4e and f. The defective structure of MWCNTs can be clearly identified by the difference in the inner and outer diameter along the tube, and coexistence of scrolls within the tubes. The external defective wall of the tubes and the scroll structure indicate the presence of functional groups at its surface and on the edges of the scroll.[46,47] At higher magnification (FFT image – inset Fig. 4f), there is an indication of a crystalline graphitic phase due to the stacking of the walls. The electronic properties of CNTs can be affected by the variation of interwall spacing. In this study, an interlayer/intershell distance of 0.31 to 0.325 nm was observed. The interwall

spacing strongly depends on the inner diameter of the tubes. The inner diameter of CNTs from 2.5 to maximum 8.7 nm was detected. The outer diameter of CNTs was in the range of 9.5 to 16.8 nm. The irregular layer spacing as a consequence of the presence of scrolls within a single MWCNT provides information about the formation mechanism of the tubes from graphene layers to scrolls and then to nanotubes through progression of defects.[47] MWCNTs have closed and empty tips. Thus, a base growth mechanism of bamboo-like MWCNTs within the pores of the matrix is proposed.

The minor phase consisting of graphene nanocages is explained by the bending of graphene sheets as an effort to eliminate the highly energetic dangling bonds present at the edges of this structure.[48]

Bright field STEM (BF-STEM, Fig. 5a) was used to assess the distribution of the elements. The composition of the sample, as measured by EDX under bright field STEM, is shown as an inset in Fig. 5a. As shown in Fig. 5b–d, the composing elements O, C and Si are homogeneously distributed in the ceramic sample. Based on this measurement, we can assume that 1D nanocarbon is embedded in the silica rich matrix and, as demonstrated for most of the PDC samples, carbon should be located in the pores of the matrix material. Looking at the outer diameter of the MWCNTs measured at the edges of the samples ($d \sim 9.5$–16.8 nm), it is reasonable to assume that the average pore size of this material should be in the same range size as the diameter of MWCNTs. No other elements were identified in this material, especially the presence of any metal which can catalyze the formation of CNTs can be ruled out. Moreover, no SiC phase was found. It seems that the silica phase plays the role of a "catalyst" in the formation of tubes and cages and its porous nature is crucial as a template for the elongation of the tubes in the matrix.

Elemental analysis. Remarkably, the sample DHBP0.1_P represents the first polymer-derived ceramic with a free-carbon phase consisting of bamboo-like multiwalled carbon nanotubes, as well as few exotic bean-like graphene nanocages. For this sample, elemental analysis was performed (Table 1). The ceramic contains a relatively low content of carbon and it is rich in silicon and oxygen, in a 1 : 2 ratio. As shown by the phase composition, the sample can be described as a SiO_2/C nanocomposite.

Fourier-transform infrared (FTIR) spectroscopy. Fourier-transform infrared (FTIR) spectroscopy is an important integral method for the characterization of the bonding situation and respectively, the microstructure of the polymers and ceramics. Fig. 6a shows the FTIR analysis of the single source precursor as well as the ceramic powder synthesized at 900 °C.

FTIR spectroscopy is usually used to probe the atomic-scale structure of silica species in glasses as well as of silicon oxycarbide ceramics, giving a direct hint to the state of the silica framework and possible bonding with the free carbon phase. Absorption bands in the range of wave numbers of 467 to 486 cm^{-1}, 800 to 812 cm^{-1}, and 1095 to 1175 cm^{-1} were assigned to tetrahedral SiO_4 units, symmetrical Si–O–Si, and asymmetrical Si–O–Si vibration, respectively. Particularly, the asymmetrical Si–O–Si valence vibration shifts significantly to lower values with an increasing number of framework defects.

Table 1 Elemental analysis and empirical formula of the ceramic sample DHBP0.1_P_900 °C

Sample name	C [wt%]	Si [wt%]	O [wt%]	H [wt%]	Empirical formula
DHBP0.1_P	11.43	41.12	46.75	0.70	$Si_1C_{0.65}O_{1.99}H_{0.48}$

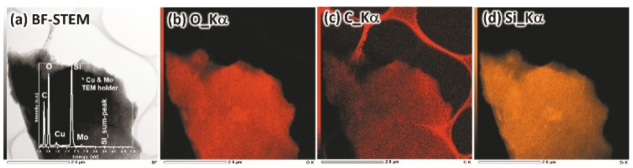

Fig. 5 (a) Bright field scanning electron microscopy (BF-STEM) image of DHBP0.1_P. Inset of EDX measured under BF-STEM. Element mapping of O_Kα (b), C_Kα (c) and Si_Kα (d) under STEM.

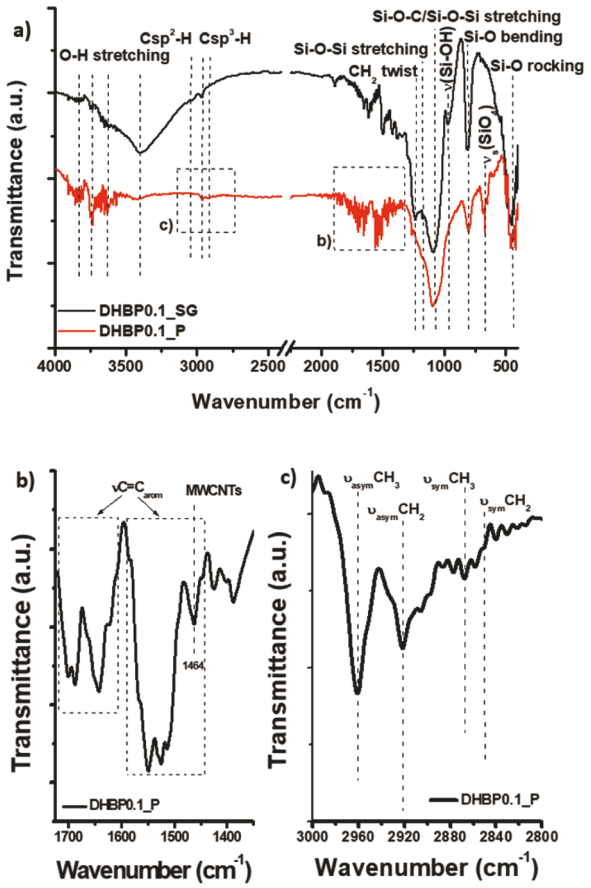

Fig. 6 (a) FTIR spectrum of single source precursor DHBP0.1_SG as compared to DHBP0.1_P prepared *via* pyrolysis at 900 °C. (b) The region corresponding to conjugated C=C vibration bands of the free carbon phase in DHBP0.1_P; (c) the presence of $-CH_2-$ and $-CH_3$ vibration modes in DHBP0.1_P. Please note the absence of any Csp^2-H bonds in ceramics.

The most intensive absorption band at 1095 cm^{-1} is also related to Si–O–C stretching vibration and indicates the covalent bonding between the silica phase and free carbon phase at the interface between nanodomains. Si–O–Si valence vibration depends also on the different bond lengths and angles in $Si(OSi)_4$, $Si(OSi)_3(OH)$ or $Si\text{-}(OSi)_2(OH)_2$ tetrahedra.

The ceramic sample prepared *via* pyrolysis at 900 °C contains Si–OH groups and also seems to adsorb a significant amount of water on its surface, as indicated by the presence of absorption bands at 3365–3850, 970 and 467 cm^{-1}, corresponding to $\nu(OH/H_2O)$ and $\gamma(OH)$ respectively. This behavior can indicate a high surface area as well as high porosity for this ceramic material. The shoulder at ~970 cm^{-1} corresponds to the stretching vibration of Si–OH bonds. There are also three other important contributions of Si–OH groups in the IR spectrum of the pyrolyzed sample, namely at 3400 cm^{-1} (symmetric feature), 3650 cm^{-1} (asymmetric feature) as well as at 3850 cm^{-1} (symmetric feature). Depending on the local environment of Si–OH groups in silica, these bands can be assigned to near-neighboring Si–OH groups with strong H-bonding interactions, to Si–OH groups that are only partially shielded from other similar neighboring groups and with very weak interactions between the H atom of Si–OH and O atoms of the Si–O–Si network and to Si–OH groups isolated from other groups, *e.g.* OH on the surface of the material, respectively.

The presence of sp^3C–H corresponding bands and the absence of sp^2C–H vibration modes are rather unusual for a ceramic synthesized at 900 °C. Normally, hydrogen is bonded to sp^2C and it was found up to very high temperatures ($T \sim 1600$ °C) in polymer-derived ceramics. In our case, sp^3C is exclusively bound to hydrogen and it should comprise the external highly defective wall of CNTs as well as the edges of graphene scrolls observed in HRTEM (Fig. 4e and f). As shown in Fig. 6c, the symmetric and asymmetric stretching vibrations of $-CH_2-$ and $-CH_3$ bands can be found in the wavenumber range of 2840–2960 cm^{-1}. The presence of the (sp^3) CH_2 twisting mode is also observed at 1260 cm^{-1}. As reported few years ago,[49] the folding of multilayer graphene to form graphene nanocages is also related to its hydrogenation of round corners. The sp^3 hybridization of carbon bonds and the resulting geometry as well as the van der Waals forces between the graphene layer and sp^3C–H bonds act together as a driving force to tackle the energy barrier of the folding process.[49]

While Raman spectroscopy is the established method for the identification of free carbon in ceramics, few FTIR studies were reported due to the poor infrared transmittance of graphene-like carbons. The reported IR-active modes of graphite are at 868 (out-of-plane vibration mode) and 1590 cm^{-1} (in-plane vibration mode). Phonon modes at 850 (radial mode) and 1590 cm^{-1} (tangential mode), independent of symmetries or diameter of carbon nanotubes, were reported previously for SWCNTs.[50,51] The radial mode vanishes in the infrared spectra of DWCNTs. As reported in the literature,[52] the number of IR active modes is independent of the nanotube diameter. However, the location of the peaks is a sensitive function of the diameter that becomes less marked for tubes with a diameter larger than 1.57 nm. Nevertheless, *ab initio* calculations predict an upshift of the frequency of this mode with the diameter of the carbon nanotubes.[52]

In the present study, the free carbon phase was formed by the thermal decomposition/rearrangement of biphenyl groups; its presence is proved by several aromatic C–C stretching vibrations (see Fig. 6b) between 1400 and 1700 cm^{-1}. A complex distribution of bands was only reported for MWCNTs and cannot be found in SWCNT- or graphite-containing materials.[53] The presence of the vibration band at approximately 1464 cm^{-1} was reported by Misra *et al.*, as being unique for MWCNTs.[54]

Micro-Raman spectroscopy. Micro-Raman spectroscopy is a powerful tool in order to identify sp^2 hybridized carbon species. The representative features of sp^2 carbon in the Raman spectra are the so-called disorder-induced D-band at approx. 1350 cm^{-1} and the G band at approx. 1582 cm^{-1} due to the in-plane bond stretching of sp^2 carbon, as well as the 2D-band (the overtone of the G-band which is always observed in defect-free samples at ~2700 cm^{-1}). Other overtones and combination bands, namely (D″ + D, D + G, 2D′) (Fig. 7), can be identified in the Raman spectra of nanocarbons. Moreover, the D and G bands can vary in intensity, position and width, depending on the structural organization of the sample under investigation. Two representative spectra were registered for the sample DHBP0.1_P, synthesized at 900 °C (Fig. 7a and their deconvolution of the frequency range 850–1800 cm^{-1} in Fig. 7b and c).

In the low-energy range, several bands resulting from the radial-like breathing modes (RLBM) of the resonantly excited graphene scrolls reported by HRTEM analysis in Fig. 4e and f, were observed. For a single walled carbon nanotube, only a single radial-breathing mode peak should be observed. The RBM frequency depends on the diameter of the tubes and is typically located between 100 cm^{-1} and 400 cm^{-1} and is often considered in the literature as their fingerprint. Nevertheless, the curvature in the graphene scrolls transforms this translation into a phonon mode similar to the radial breathing mode in SWNTs. As shown in the inset of Fig. 7a, RLBM bands were found at 99, 122 and 139 cm^{-1} (in DHBP0.1_P). As reported in the literature, the edges of graphene scrolls are playing an important role in the activation of RLBM bands.[55]

The multiwalled carbon nanotubes (MWCNTs) are composed of multiple concentric graphite cylinders. Their Raman spectra depend on their crystalline arrangement given by the A_D/A_G ratio, which is commonly taken as a measure of the graphitization index and reflects the concentration of structural defects and the A_{2D}/A_D ratio which is sensitive to the overall crystalline quality of the graphitic network and increases with long-range ordering.[56]

The Raman spectrum of MWCNTs shows a high A_D/A_G ratio and low A_{2D}/A_D ratio. The position of the G band in MWCNTs is somehow higher (~1605 cm^{-1}) than that of other carbonaceous materials, and this was associated with a large compressive stress affecting the C=C bonds in highly defective tube walls. Nevertheless, this apparent blue shift of the broadened G band may be explained as well by an overlap with the

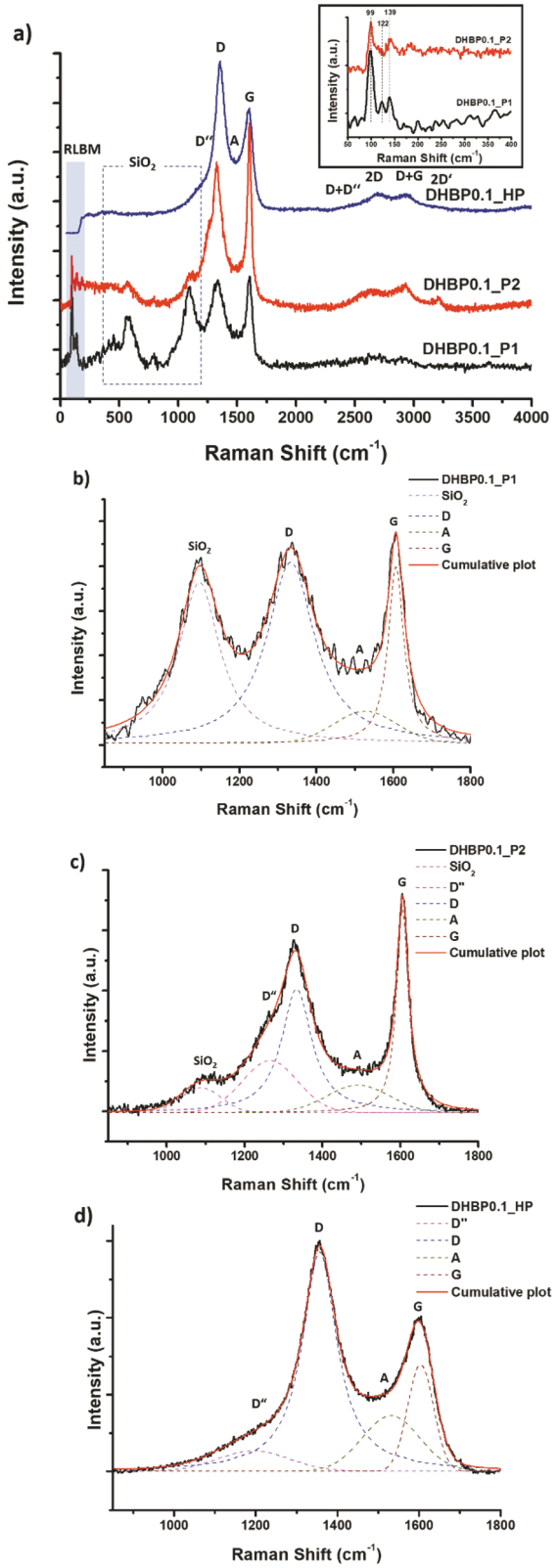

Fig. 7 Micro-Raman analysis of the ceramic sample as prepared at 900 (2 distinctive profiles, DHBP0.1_P1 and DHBP0.1_P2) and 1600 °C (DHBP0.1_HP). Fitting of the region 850–1800 cm^{-1} for (b) DHBP0.1_P1, (c) DHBP0.1_P2 and (d) DHBP0.1_HP.

unresolved D′ band at 1610 cm^{-1}, which is also a disorder-induced double resonance process and is often found in nanocrystalline graphite. Its overtone band, 2D′, can be identified in the frequency range of 3200–3246 cm^{-1} for all samples.

The slightly disordered state indicated by the existence of both bands D″ (shoulder at ~1200 cm^{-1} attributed to the presence of sp^2–sp^3 C–C and C=C bonds) and A (at ~1500 cm^{-1}, corresponding to the fraction of amorphous carbon contained in the samples) correlates to the presence of edges in the graphene scrolled layers, by the deviation from planarity of graphene layers, by the presence of pores, and by the presence of carbon atoms with sp^3 hybridization, as shown previously in the FTIR and HRTEM discussion.

The intensity ratio of the D and G modes, A_D/A_G, enables the evaluation of the carbon-cluster size by using the formula reported by Cançado[57] (eqn (1))

$$L_a(\mathrm{nm}) = \frac{560}{E_L{}^4}\left[\frac{A_D}{A_G}\right]^{-1} \quad (1)$$

with L_a being the size of the carbon domains along the six-fold ring plane (lateral size between line defects) and E_L the energy of laser used in the study (2.41 eV corresponding to 514.5 nm laser wavelength). Lorentzian and Gaussian curve fitting of the Raman bands was performed in order to extract the A_D/A_G intensity ratios and to determine the size of the free carbon cluster formed in the ceramics. The peak fitting was done including the minor bands D″ and A.

The dependence of the A_D/A_G ratio on the degree of disorder in graphene-like materials was also reported.[58] The disorder was quantified as depending on point-like defects, precisely on the inter-defect distance, L_D, which can be calculated using eqn (2). Pristine graphene has $L_D \to \infty$, and fully disordered graphene has $L_D \to 0$.

$$L_D(\mathrm{nm}) = \sqrt{\frac{4300}{E_L{}^4(\mathrm{eV}^4)}\left[\frac{A_D}{A_G}\right]^{-1}} \quad (2)$$

where the average distance between point defects and the defect density ($\sigma = 1/L_D{}^2$) can be calculated. In this study, the defect density of the ceramic at 900 °C, $\sigma_{900\ ^\circ C} = 0.02$ is compared to that at 1600 °C where a value of $\sigma_{1600\ ^\circ C} = 0.03$ was calculated. A slightly higher value of defect density can be registered for the sample hot-pressed at 1600 °C indicating that the applied temperature and pressure influenced the carbon structure, creating more defect states at higher temperature.

The average continuous carbon precipitate size, including tortuosity, can be determined using eqn (3) as described by Larouche *et al.*:[59]

$$L_{eq}(nm) = 8.8 \cdot \left(\frac{A_{2D}}{A_D}\right) \quad (3)$$

The inter-defect distances L_D, lateral cluster size L_a, and the tortuosity parameter L_{eq} together with the ratio of D and G, 2D and G and are summarized in Table 2.

Complementary to FTIR, Raman spectroscopy can be used for the identification of the molecular structure of the silica

Table 2 Raman graphitization parameters for the samples prepared at 900 °C (DHBP0.1_P1 and DHNP0.1_P2) and hot-pressed at 1600 °C (DHBP0.1_HP)

Sample	ω_D[a] [cm^{-1}]	ω_G[a] [cm^{-1}]	ω_{2D}[a] [cm^{-1}]	A_D/A_G	A_{2D}/A_G	L_a [nm]	L_D [nm]	L_{eq} [nm]
DHBP0.1_P1	1335.7	1606.5	2660.8	2.95	0.64	5.63	6.57	1.90
DHBP0.1_P2	1334.0	1605.4	2646.5	1.92	0.66	8.63	8.14	3.04
DHBP0.1_HP	1356.6	1603.6	2797.2	3.99	0.63	4.16	5.65	1.38

[a] Where ω represents the wavenumber position of the respective Raman bands.

phase in this study. As seen in Fig. 7a, different Raman bands corresponding to the SiO_2-phase are present in DHBP0.1_P ceramics. They can be found at 1095, 795, 568 and 452 cm^{-1}. The bands at 452 and 568 cm^{-1} are attributed to the rocking and bending vibration (ν_b) of Si–O–Si linkages, respectively. The band at 795 cm^{-1} is related to the symmetric stretching vibration (ν_s) of Si–O–Si. The band with maxima at 1095 cm^{-1} is assigned to the transverse optical asymmetric stretching vibration (ν_{as}) of Si–O–Si linkage or/and Si-OC units. The broad and intensive Raman band at 1095 cm^{-1} in DHBP0.1_P1 can be attributed also to the stretching vibration of the Si–O bond of SiO_4 tetrahedral units with one NBO (OH), *i.e.* Q^3 SiO_3(OH) structural units.

To conclude, the vibrational spectroscopy studies indicate the presence of defective (bamboo-like) MWCNTs observed by HRTEM. The observation of low-frequency radial breathing-like modes by Raman spectroscopy confirms that the curvature in the scroll activates new modes that are absent in folded or flat graphene. The graphene scrolls have a large concentration of saturated –CH_3 and –CH_2– containing edges, as revealed by FTIR analysis as well as Raman spectroscopy.

Brunauer–Emmett–Teller (BET) analysis. The porosity and specific surface area of pyrolyzed ceramics at 900 °C as compared to silica were evaluated *via* nitrogen adsorption studies (Fig. 8 and Table 3). It has been observed that the specific surface area decreases with the incorporation of the carbon phase into DHBP0.1_P, indicating that the carbon phase is located in the pores of the matrix. This observation was previously done in several polymer-derived ceramics.[38]

DHBP0.1_P is a mesoporous ceramic nanocomposite (isotherm IVa) with a relatively large specific surface area, and therefore suitable for a whole range of applications such as gas adsorption, gas separation and catalyst support. It can be observed that already a very low concentration of biphenyl induces a decrease in the specific surface area of the ceramic and in the average pore size. Due to its relatively high specific surface area, the ceramic can adsorb a large concentration of water in its pores, as observed by FTIR analysis for the formation of silanol units.

The hysteresis loop scanning gives information on the interconnectivity of the pores as well as on the geometry/shapes of the pores. In the case of DHBP0.1_P, the curvature upon decompression is less steep compared to that of silica samples. This hysteresis appearing in the multilayer range of physisorption isotherms is usually associated with capillary condensation in mesopore structures. N_2 isotherms of type IVa

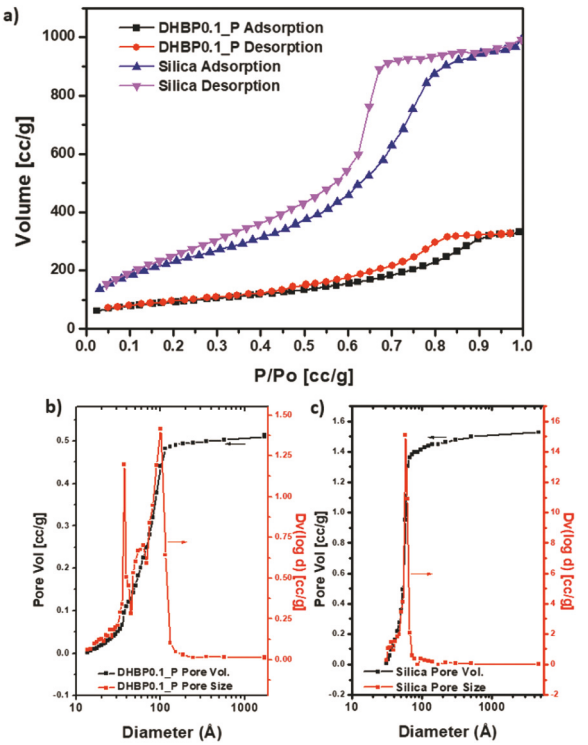

Fig. 8 (a) BET isotherm analysis of DHBP0.1_P as compared with silica. Pore size distribution and pore volume for (b) DHBP0.1_P and (b) silica. Please note that both samples were produced by pyrolysis at 900 °C under an argon atmosphere.

Table 3 Nitrogen adsorption data for DHBP0.1_P as compared with silica produced *via* pyrolysis at 900 °C

Sample name	Specific surface area [m^2 g^{-1}]	Average pore size [Å]	Pore volume [cm^3 g^{-1}]
Silica	637	74	1.53
DHBP0.1_P	371	62	0.51

accompanied by a type H2 hysteresis loop, according to IUPAC classification, are indicating a more random distribution of pores and an interconnected pore system. Thus, a different behavior of the adsorption and desorption branch of the isotherm, in particular around $p = p_0/p_0 = 0.45$ (for N_2 at 77 K), leading to a forced closure of the hysteresis loop is registered. The tensile strength effect of $(p/p_0)_{TSE}$ of 0.46182 was calculated for DHBP0.1_P. As shown in Fig. 8b and c, the pore sizes

of DHBP0.1_P are in the same range as the external diameter of DWCNTs observed by micro-Raman spectroscopy as well as MWCNTs identified by HRTEM analysis.

Electrical conductivity. The existence of a continuous network of carbon nanotubes was proved by four-probe measurements at room temperature. Astonishingly, the monolithic hot-pressed DHBP0.1_HP sample, containing only 11.43 wt% free carbon, showed a specific resistance of 4.588×10^{-4} Ωm, corresponding to an electrical conductivity value of 2.179×10^{3} S m^{-1}. This surprisingly high value for the electrical conductivity can be explained only by the nature of the nanocarbon phase in the structure. As a comparison, another amorphous SiOC ceramic with a similar content of carbon but a different type of free carbon phase, namely the multilayer-graphene like phase, and hot-pressed in the same way at 1600 °C, shows an electrical conductivity of approximately 10^{-2} S m^{-1} (for 13.95 wt% C).[60]

As previously indicated in this paper, the nanocarbon phase is made of multiwalled carbon nanotubes and carbon nanocages. The nanotubes are growing through the pores (voids) of the silica matrix, as indicated by the BET analysis as well, and form an interconnected network. As compared with ref. 60, the presence of an interconnected 1D nanocarbon phase can explain the great electrical conductivity of this material.

Energetics. The pyrolyzed ceramic at 900 °C was analyzed by means of high temperature oxide melt calorimetry. Through calculation by using proper thermocycles, the standard oxidation enthalpies at room temperature and standard formation enthalpies at room temperature are obtained and listed in Table 4.

For comparison, the energetics of compounds with similar elemental compositions but different structures are tabulated as well. According to the structural analysis discussed previously, it was found that carbon nanotubes are formed in the voids of the silica matrix, so it is reasonable to compare the energetics of this CNT-silica composite with a mixture of amorphous silica and carbon nanotube/nanocages with similar structures (diameters, number of layers and other structural features). Table 5 shows the energetics of several carbon allotropes as well as various silica forms for reference. Considering the following reaction, the standard enthalpy of this reaction depends on the choice of silica and carbon forms.

$$0.2427\ SiO_2 + 0.1578\ C + 0.0576\ H_2\ (g) \rightarrow D0.1P$$

In this context, it is important to note that thermodynamic functions strongly depend on the number of carbon layers, defectiveness and presence of heteroatoms.[61] The enthalpy of formation of multi-walled CNTs strongly depends on their structure. The enthalpy of formation of multi-walled CNTs with cylindrical and conical structures is 8.60 ± 0.52 and 21.70 ± 1.32 kJ mol^{-1}, respectively.[62] No data are available for the minor carbon nanocage phase in this ceramic, thus, the discussion will focus on CNTs. As for silica, the energetics are strongly dependent on the crystallinity and surface area. We can choose two end situations to discuss, the most and the

Table 5 Room temperature oxidation enthalpies and standard enthalpies of formation at room temperature of various carbon nanotubes and various silica forms, together with their reported specific surface area (SSA)

Sample	$\Delta H_{ox,\ 25\ °C}$ (kJ mol^{-1})	$\Delta H_{f,\ 25\ °C}$ (kJ mol^{-1})	SSA (m^2 g^{-1})
Graphite		0	
SWCNTs[66]	−393.52 ± 0.05	7	
Cylindrical MWCNTs[62]	−395.42 ± 0.50	8.6	
Herringbone MWCNTs[62]	−432.76 ± 0.19	21.70	
SiO_2 (cristobalite)[67]		−908.4 ± 2.1	
SiO_2 (amorphous)[68]		−895.52	198.08
SiO_2 (amorphous)[68]		−910.86	25.11

Table 4 Energetics of DHBP0.1_P as compared to other SiOC ceramics reported in the literature

	Atomic percentage (%)							
	Si	O	C	H	ΔH_{ds}/kJ g^{-1}-at.	$\Delta H_{ox,\ 25\ °C}$/kJ g^{-1}-at.	$\Delta H_{f,\ ele}$/kJ g^{-1}-at.	$\Delta H_{f,\ com}$/kJ g^{-1}-at.
DHBP0.1_P	24.27	48.44	15.78	11.51	−40.58 ± 0.44	−58.13 ± 0.44	−232.65 ± 0.99	−12.60 ± 1.51
SiOC1[63]	36.4	51.3	12.3	—	−101.2 ± 7.1	−118.3 ± 7.1	−260.5 ± 7.1	−19.8 ± 7.1
	29.5	44.0	26.5	—	−143.4 ± 7.0	−159.6 ± 7.0	−212.5 ± 7.0	−7.3 ± 7.0
	27.1	37.4	35.5	—	−159.7 ± 7.2	−175.6 ± 7.2	−210.1 ± 7.2	−34.2 ± 7.2
	27.8	27.8	44.4	—	−257.0 ± 7.0	−273.0 ± 7.0	−154.1 ± 7.0	−17.8 ± 7.0
	25.9	23.8	50.3	—	−170.9 ± 7.1	−186.6 ± 7.1	−246.4 ± 7.1	−128.2 ± 7.1
SiOCH2[64]	22	32	20	26	−110.1 ± 3.10	−129.90 ± 3.10	−185.80 ± 3.60	−36.06 ± 4.31
SiOCH3[42]	34.5	52.3	8.8	4.4	−80.1 ± 3.20	−97.68 ± 3.20	−256.64 ± 3.96	−12.98 ± 5.03
	31.8	48.5	19.2	0.5	−116.5 ± 2.20	−133.02 ± 2.20	−232.12 ± 2.91	−6.31 ± 3.90
SiOCH4[65]	37.1	0.3	36.3	26.3	−458.32 ± 5.80	−479.94 ± 5.80	−37.50 ± 6.62	−9.57 ± 8.91
	25.4	19.6	22.6	32.5	−211.04 ± 2.79	−232.40 ± 2.79	−133.71 ± 3.36	−33.27 ± 4.54
	18.5	25.6	17.7	38.3	−149.95 ± 1.21	−171.52 ± 1.21	−120.92 ± 1.63	−0.47 ± 2.26
	16.4	26.1	15	42.5	−101.71 ± 1.45	−123.75 ± 1.45	−144.98 ± 1.82	−23.98 ± 2.31
	36.1	45.2	10	8.6	−94.61 ± 0.65	−113.10 ± 0.65	−266.47 ± 1.44	−53.85 ± 2.23

least thermodynamically stable combination of the reactants. For the thermodynamically most stable case, that is SiO_2 as cristobalite and C as the most stable CNT, the standard enthalpy at room temperature of the reaction above is approximately −12.9 kJ mol^{-1}, which means that DHBP0.1_P is actually energetically more stable than the most stable mixture. As for the least thermodynamically stable case, the standard enthalpy at room temperature becomes even more negative, indicating that the formation of DHBP0.1_P is energetically favorable.

Moreover, even when we use graphite as the reactant, the standard enthalpy of the reaction above is −12.6 kJ mol^{-1}, meaning that it is still energetically favorable to form DHBP0.1_P. This tells us that there are other sources of energetics benefits from the formation of DHBP0.1_P. Looking back at the structural analysis, the strong covalent bonds at the interface between the free carbon phase and amorphous silica phase can account for this energetics benefits, which is similar to the mixed bonds found in PDCs. Another possible source is the existence of sp^3C–H bonds which is unusual after pyrolysis under 900 °C, as well as the existence of Si–OH bonds in the structure. The sp^3C–H bonds presented at the highly defective walls of MWCNTs inside the pores of the silica matrix can saturate surface bonding and eliminate defects, such as dangling bonds. Similar to SiOCH presented in Table 4 for comparison,[65] these sp^3C–H bonds can convey the system with more thermodynamic stability. However, unlike other PDC or low-*k* SiOCH listed in Table 4, there is a substantial number of Si–OH bonds found in the structure of this DHBP0.1_P sample. This can be attributed to the fact that the silica matrix of this DHBP0.1_P sample contains Si–OH network units and also has a very high surface area and is likely to adsorb water into the structure. The chemisorbed water forms Si–OH bonds with the amorphous silica matrix, and this fact confers the system with extra energetics benefits.

Weak chemical interactions such as van der Waals forces, hydrogen bonding and π–π interactions should affect the enthalpy of DHBP0.1_P, even if their contribution is minor. Nevertheless, π-stacking for example, a weak-yet-strong chemical interaction, plays a major role in stabilizing the architecture of this compound.

In our study, the formation of defect-rich bamboo-like MWCNTs is explained by the presence of a porous silica matrix. As shown in 2009, a major breakthrough in the carbon nanotube science was made by few reports on CH_4- or ethanol-CVD (900 °C for 10 min) which have shown that silica can act as catalytically active nucleation point for SWCNT formation.[27,28,35] Silica is neither able to dissolve carbon nor catalyze the decomposition of hydrocarbons. The surprising catalytic activity of silica was explained by the mobility of Si and O atoms in molten SiO_2 which can cause the intermediate formation of holes or defects, strongly enhancing the catalytic capacity to decompose hydrocarbons. Moreover, the curved surface of silica nanoparticles can act as a template for the formation of a graphitic hemispherical nanotube end cap. Therefore, the catalytic function of silica is size dependent, and only small nanoparticles (diameter <2 nm) are active as nucleation sites.

Furthermore, the high concentration of hydrogen induces the highly defective structure of the nanotubes. The same issue was observed in the case of CVD processes. In the case of CVD processes, the presence of hydrogen normally accelerates the CNT growth and favorably produces the bamboo-like microstructures.[69] Moreover, the formation of bamboo-like microstructures was related to a fast CNT growth. The formation of well graphitized crystallized CNTs usually needs a long(er) time.

The diameter of the tubes seems to depend on the pore sizes of the silica matrix. As reported in 2008, CNTs can be formed also in a porous alumina matrix (40 nm pore size) by using the CVD method.[31] The homogeneous distribution of elements in the matrix, as shown by EDX element mapping under STEM, indicates that the nanotubes are forming an interconnected network in the pores of the entire matrix, information indicated also by the extremely high value for the electrical conductivity.

The formation of the nanotubes from a carbon-rich polysiloxane is attributed to an early phase separation of the carbon-phase from the silica phase, formation of nanorings[70] followed by physical vapor elongation and self-assembly in the mesoporous silica matrix.

Our experimental studies were paralleled by computational efforts providing detailed atomistic simulations of the formation mechanism.

Density functional theory calculations

Models of SiO_2 and stoichiometric SiOC glass (Si_5CO_8) containing additional "free" carbon have been generated with *ab initio* molecular dynamic simulations through a variety of procedures. We either cooled or heated random arrangements of Si, C, and O to observe structure formation. Consistently we find that "free" carbon segregates into planar sheets extending throughout the unit cell. This essentially creates slab models with a carbon layer separated from a glass layer. The genesis of planar carbon structures, the quality of the glass structure, and the enthalpy of formation of the complete models generally depend on cooling or heating rates. As a caveat, we note that models with 112–152 atoms extend only 1.2 to 1.5 nm, and that periodic boundary conditions may impact structure formation. Nevertheless, the findings motivated a series of further investigations, in particular the force-field simulations described further below. In models of SiO_2 with "free" carbon we observe almost exclusively Si–O and C–C bonds only. This implies that SiO_2 and C (almost) separate. Interestingly, most models are void of C–O bonds unless an excess of O atoms is present. Eventually this yields C–O bonds at the edges of carbon segregations. Few Si–C bonds appear at the edges of carbon segregations. Models with an excess of O, *e.g.* SiO_3C_2, develop CO and CO_2 until the composition SiO_2 : C is reached, with only small deviations from an "ideal" SiO_2. Summarizing, the key observation from structure simulations *via* DFT is the development of carbon segregations ("graphene layers") without covalent bonds perpendicular to their surface normal.

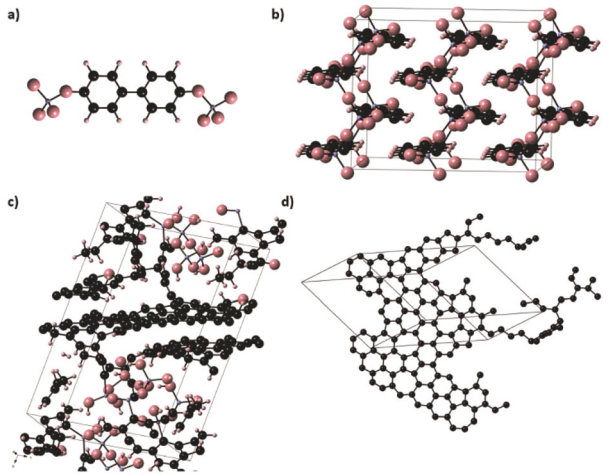

Fig. 9 Polymer fragment (a) used to build periodic models. Optimized structures obtained from *ab initio* molecular dynamics simulations of heating a model of the DA-polymer at 1200 K (b) and 3000 K (c). The extended carbon arrangement found in the 3000 K model (d). The simulation was performed for about 150 ps under constant pressure allowing the cell to change its shape, though the density remained almost constant (r = 1.6 g cm^{-3}) throughout the simulation. The composition is $Si_8O_{24}C_{96}H_{64}$ and no gaseous species were removed during the simulation.

We encounter the development of carbon segregations when annealing a model of DHBP0.1_SG as well. We built a periodic model of the polymer, see Fig. 9, and annealed this in constant pressure *ab initio* molecular dynamic simulations. No particles were removed during the simulation, so the optimized models contain some H_2 and CO, but also larger hydrocarbons (C_4H_8). Prevalent, however, is the extended carbon segregation that was formed by fusing bis-phenol rings together. It combines almost all carbon atoms of the model into one joint fragment.

Empirical potential simulations

Throughout our empirical potential simulations of SiOC we observe a characteristic development of structures upon annealing. In Fig. 10 we show this for models with composition $SiO_2 : C_{0.5}$, which mimics the experimental data reported in Table 1. Fig. 10 only shows the carbon atoms of the SiOC structure, with Si and O atoms omitted for clarity. At low temperatures, we observe small carbon fragments dispersed in the model. Typical is the appearance of C_6-rings which have joined to small aromatic units. Increasing the temperature fuses many such small fragments *via* edges to form pieces of graphene sheets. At this stage, some sheets already show curvature. A further increase of temperature produces balls and tubular structures. The amount of "free" carbon impacts the spatial extension of the carbon fragments, see Fig. 11. In models with low carbon content, graphene sheets appear isolated and do not form a continuous network. Hence, they are embedded in a continuous glass phase. For structures with higher C content the graphene sheets form extended networks

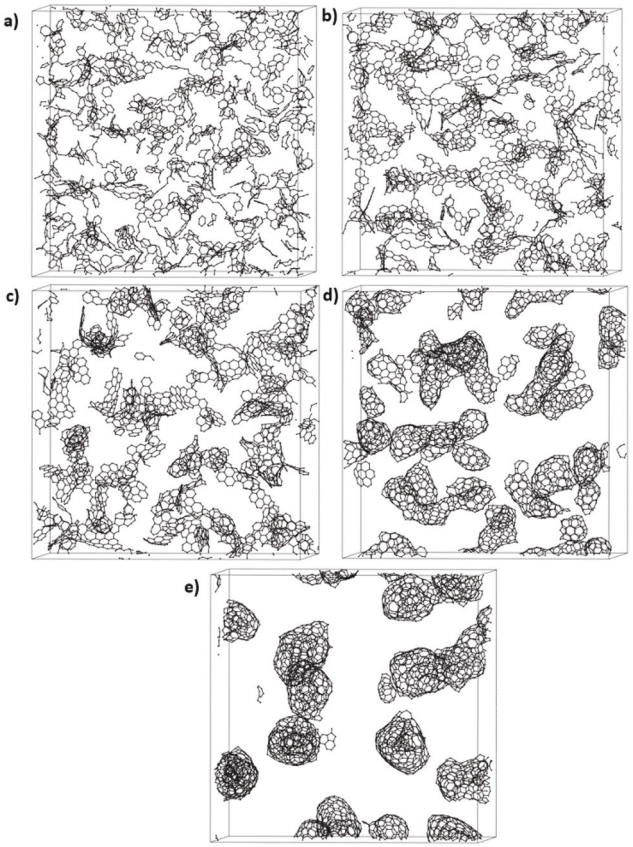

Fig. 10 Carbon structures in SiOC for the composition $SiO_2 : C_{0.5}$, C : Si = 1 : 2 obtained in empirical potential simulations. Only C atoms are shown, Si and O have been omitted. The sequence of pictures corresponds to annealing at increasingly higher temperature (parameter T_{MC} in MC-simulations). The size of the (periodic) simulation box is 7.4 nm and the density of all SiOC models is 2.2 g cm^{-3}.

that resemble funnel-webs of certain spiders (*e.g.* Agelenidae). The principle characteristic is again the formation of sheet-like structures separated by and embedded in a glass phase. At higher temperature, these sheets coil up to form balls or tubular structures. Depending on the amount of "free" carbon, the carbon tubes may form a continuous network. These are still embedded in a continuous glass phase. Hence, carbon segregation and glass phase form a bi-continuous system. Our simulations described here yield characteristic diameters of tubular carbon segregations of 1–2 nm. Interestingly, these diameters as well as the typical distance between sheet-like graphene, hence the thicknesses of the glass between carbon segregations, relate to typical scattering lengths observed in SANS and SAXS experiments.[71]

Reactive-force-field simulations

To bridge the gap between accurate density functional theory calculations with *ab initio* simulations and empirical potential molecular dynamics simulations, we recently developed a new reactive force field (ReaxFF[72]) capable of describing properly the energy and structure of amorphous silicon oxycarbide.[73]

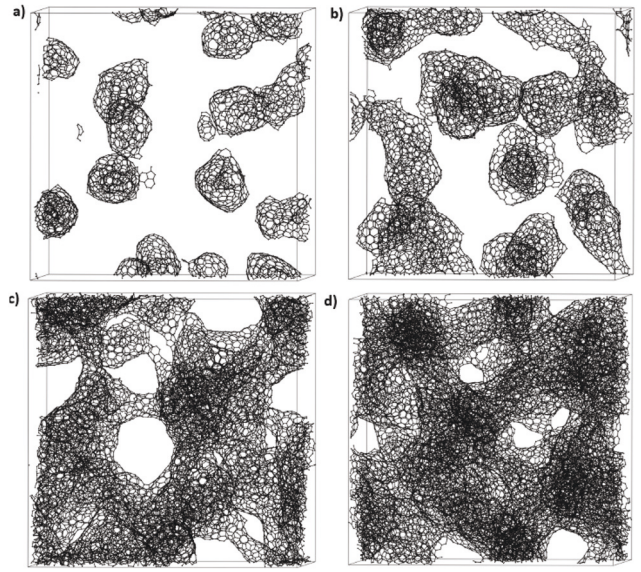

Fig. 11 Carbon structures in SiOC obtained at high annealing temperature in empirical potential simulations. The amount of "free" carbon increases in the sequence, C : Si = 0.5, 1, 2, 3. Only C atoms are shown, while Si and O have been omitted. All models exhibit a density of 2.2 g cm^{-3} and the size of the (periodic) simulation box increases from 7.4 to 8.4 nm with increasing carbon content.

Fitted extensively to quantum-chemical calculations, the reactive force field achieves an accuracy comparable to DFT calculations at a significantly lower computational cost. This allows simulations of large systems for a long time with high fidelity, and is particularly well suited to investigate the polymer-to-ceramic processes.[73]

We investigated the formation of amorphous silicon oxycarbide using ReaxFF using a variety of approaches, including melt-quench simulations and heating polymer structures. Fig. 12 shows outcomes, which on one side match *ab initio* MD simulations and on the other side connect up to empirical potential simulations.

Phase development in small models (100–200 atoms) follows the same patterns in reactive force field simulations as in *ab initio* molecular dynamic simulations: "Free" carbon segregates into sheet-like structures. Depending on the composition, a small fragment is embedded in silica or an extended sheet separates thin glass layers, see Fig. 12. Larger models exhibit carbon sheets with high curvature. Depending on the composition, the sp^2-carbon structures resemble fragments of multi-walled tubular carbon structures (Fig. 12, right).

Mimicking the processing of DHBP0.1_SG we performed the described simulation several times. Although outcomes vary slightly, final structures show the same features as shown in Fig. 13. We observe bean-like segregations of silica (in the model shown in Fig. 13, approximately 6 nm long and 2 nm wide). Carbon atoms "surround" the silica segregations forming various curved carbon fragments. As seen in Fig. 13, hydrogen terminates the carbon segregations at various places and may impact further condensation of graphene.

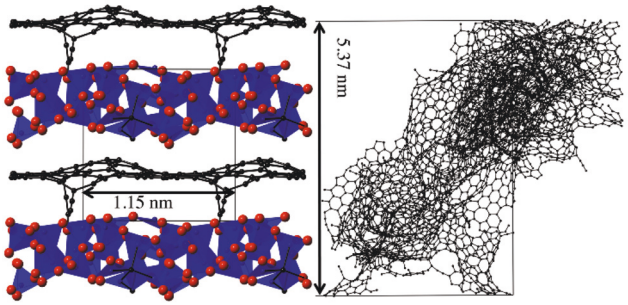

Fig. 12 Amorphous silicon oxycarbide models (composition Si_5CO_8 + 10C; density 2.2 g m^{-3}) generated *via* melt-quench simulations using the reactive force field. On the left a small 120-atom model showing graphene sheet segregated between "glassy" SiOC. Box sizes of this model are ~1.2 nm. On the right the "free" carbon structure in a 12 288-atom model (box sizes ~5.4 nm). Si and O are not shown in this model for clarity.

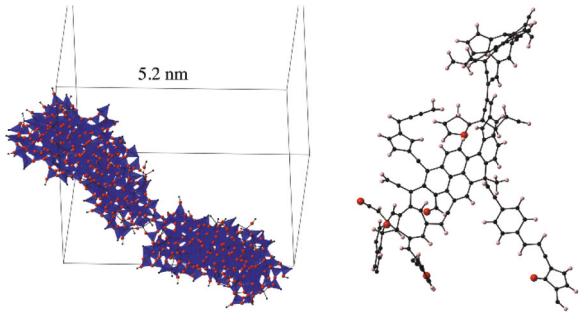

Fig. 13 SiOC structure obtained through reactive force field simulations after annealing DHBP0.1_SG. (left) Two segregated silica beans; (right) a typical fragment of carbon with curvature.

Unfortunately, mass loss and removal of similar proportions of the initial polymer like in the experiment (Table 1 indicates that 95% of all carbon is lost) appears unfeasible at the time-scales available (~1 ns) to the simulation: we only removed about 30% of H atoms and ~25% of C atoms as gas molecules. Careful analysis of trajectories shows that during initial heating DHBP0.1_SG tends to dissociate into siloxane and DHBP. Experimentally, DHBP is volatile at 900 °C. Thus, DHBP and its fragments are most likely species lost during annealing, and, consequently, the major source of mass loss. In simulations, however, we don't remove such big fragments, and these become part of the continuous carbon phase, eventually. This difference between experiment and simulation does not impact the general trends.

Conclusions

In summary, we propose a simple and effective method for the formation of metal-catalyst-free bamboo-like MWCNTs in a mesoporous silica matrix using the polymer-derived ceramic process. The influence of the initial structure of the precursor, the low temperature of the phase separation and the role of

the silica particle sizes and the pore sizes on the formation and microstructural particulars of bamboo-like MWCNTs was discussed. The influence of hydrogen on the bamboo defective structure was highlighted as well. The MWCNTs are formed through a base growth mode within the silica mesoporous structure. The pores are interconnected; therefore, the uniaxial hot-pressed sample shows a very high electrical conductivity of 2.179×10^3 S m^{-1} for only 11.43 wt% carbon in its composition. To our knowledge, this is the highest value reported so far in the literature for SiOC ceramics as well as for MWCNT/SiO_2 composites. In this study, no silicon carbide was formed after hot pressing at 1600 °C. The carbothermal reduction of silica was suppressed due to several reasons: (i) a high pressure during hot pressing is known to shift the start of the reaction to higher temperature; (ii) a low carbon content is detrimental and (iii) mesoporosity plays a key role in the carbothermal reduction reaction, namely the interconnected mesoporous network provides diffusion paths for gaseous CO and SiO and confines SiC growth inside the nanocomposite.

As shown by high-temperature oxide melt calorimetry, the formation of MWCNTs in a silica matrix is energetically favorable. The thermodynamic stability of the composite is explained by the interface bonding between the silica phase and carbon and by the presence of saturated C–H bonds (on the surface of nanotubes, at edges of graphene scrolls and on the corners of nanocages) as well as silanol units in silica pores.

These new findings further confirm that the polymer-derived ceramic route can be used as an efficient tool in order to create well-defined carbon-containing nanocomposites just by simple tailoring of the chemical structure of the precursors.

Computational simulations corroborate the formation of tubular carbon apart from silica. Atomistic simulations on three different length scales show a consistent picture of carbon segregating from the amorphous glass matrix. The partitioning into two distinct phases is enhanced by the structure of the polymer, which provides ample intrinsic oxygen for reactions during the polymer-to-ceramic conversion.

To conclude, due to their exceptional properties, such as high electric conductivity, porous structure, high specific surface area, *etc.*, these materials can find applications in several fields such as vehicle/aircraft technology, health & safety, energy storage and conversion, air/water pollution control, airspace applications, *etc*.

While this study remains the first to be related to the catalyst-free generation of carbon nanotubes in PDCs, systematic studies are needed to understand the synthesis–structure–property relationship of these ceramics, particularly variation in parameters such as the polymeric precursor, chemical composition of ceramics, thermolysis temperature, and free carbon content.

Materials and methods

Synthetic procedure

All chemicals were obtained from Sigma Aldrich and used as-received. 4,4′-Dihydroxybiphenyl (DHBP) 97%, tetramethyl orthosilicate (TMOS), methanol and ethanol were provided from Sigma-Aldrich and used as received. The biphenyl-containing single-source precursor was prepared using 0.1 wt% of DHBP with respect to TMOS. The sol was prepared upon adding ethanol and TMOS to a dispersion of DHBP in water. The gelation process was performed at 60 °C and the as-obtained wet gel was placed into a drying cabinet at 60 °C and allowed to age for 5 days. The resulting xerogel (DHBP0.1_SG) was first dried under vacuum at room temperature. The same procedure was used in order to prepare a standard silica sample, using TMOS, water and ethanol. A subsequent pyrolysis process was conducted at 900 °C under an argon atmosphere (100 °C h^{-1} heating rate, 2 h dwelling time) (sample name: DHBP0.1_P, silica). The pyrolyzed powder was uniaxially hot-pressed in graphite dies into a monolith (labeled DHBP0.1_HP) (KCE hot press HP W 150/200, argon atmosphere, 30 MPa, T = 1600 °C). In order to avoid carbon diffusion into the sample from the graphite dies, its walls were covered with boron nitride.

Characterization

FTIR spectroscopy was performed on a Bruker Vertex 70/70v spectrometer.

Micro-Raman spectra were recorded using a Horiba HR800 micro-Raman spectrometer (Horiba Jobin Yvon, Bensheim, Germany) equipped with an Ar^+(514.5 nm) laser. The excitation line has its own interference filter (to filter out the plasma emission) and a Raman notch filter (for laser light rejection). The measurements were performed with a grating of 600 g mm^{-1} and a confocal microscope (magnification 100×, NA 0.5) with a 100 μm aperture. The laser power (*ca.* 20 mW) on the sample was attenuated in the range of 2 mW–20 μW using neutral density (ND) filters. The minimum achievable laser spot diameter is approx. 0.69 μm. The laser spot size is primarily defined by the laser wavelength and microscope objective being used. The minimum achievable spot size is diffraction limited, according to the laws of physics and optics: laser spot diameter = 1.22λ/NA, where λ is the wavelength of the laser, and NA is the numerical aperture of the microscope objective being used (in this case 0.90/100×). Thus, the theoretical diffraction limited spatial resolution which is achievable using an optical microscope is defined as spatial resolution = 0.61λ/NA, in this case being 0.348 μm. Nevertheless, this value is strongly influenced by the scattering of the laser/Raman photons and interaction with interfaces in the sample, issue which can reduce this resolution. Two different holographic notch filters were used for the pyrolyzed samples, compared to the hot-pressed ceramics. The pyrolyzed ceramics were re-measured with a novel 514.5 nm laser which takes advantages of the Ultra-Low Frequency (ULF) module, giving access to ultralow frequency down to 5 cm^{-1} on the LabRAM HR spectrometer. The hot-pressed sample was characterized with the old-setup having an edge of notch filter at about 170 cm^{-1}.

X-ray diffraction measurements were performed on a Bruker D8 Advance diffractometer (Bruker, USA) and on a

Seifert PTS 3003 diffractometer for powders and monoliths, respectively.

The electrical properties of the samples were assessed using four-point resistance measurements (Keithley 2400 devices).

The silicon, carbon, oxygen and hydrogen contents were determined at Mikroanalytisches Labor Pascher (Remagen, Bendorf-Germany).

N_2 adsorption was performed at −196 °C using an Autosorb-3B (Quantachrome Instruments, USA). The samples were preheated at 150 °C for 24 h under vacuum before the measurements. The pore size distributions were derived from the desorption branch of the isotherms using the Barrett–Joyner–Halenda (BJH) method.

Transmission electron microscopy (TEM) of the powder ceramics was performed using a JEOL-2010F instrument (JEOL Ltd, Tokyo, Japan) operating at an acceleration voltage of 200 kV (wavelength λ = 2.51 pm). For TEM sample preparation, the ceramic powders were dispersed in an ultrasonic bath (high purity methanol 99.5%, Wako Chem. Ltd, Japan) and a small droplet of the suspension was placed on a holey carbon (Cu) grit. Chemical analysis was performed using scanning transmission electron microscopy (STEM) and a nano-probe X-ray energy dispersive spectrometer (EDS) with a probe size of 1.5 nm.

Calorimetry

The enthalpy of formation of DHBP0.1_P was measured using high temperature oxidative molten salt solution calorimetry. A sample (~1–2 mg) was pressed into a pellet and dropped into molten sodium molybdate ($3Na_2O{\cdot}4MoO_3$) solvent at 800 °C in an AlexSYS Setaram microcalorimeter. Oxygen gas ~5 mL min^{-1} was constantly bubbled through the solvent in order to warrant full oxidation and also to stir the melt. The gaseous byproducts were flushed out of the system with an oxygen flow of ~40 mL min^{-1}. Statistically reliable data (within two standard error) were obtained by dropping at least eight pellets. The calorimeter was calibrated against the heat content of platinum. This methodology has been used in our previous reports on similar materials[65] and is well established.[74–76]

Modeling

For modeling of polymer-derived silicon oxide ceramics we apply three different methods of atomistic simulations, each acting on its own length scale. The smallest length scale is addressed by Density Functional Theory (DFT) calculations, including *ab initio* Molecular Dynamic (aiMD) simulations. Using aiMD simulations we generate and investigate SiOC models on a length scale between 1 and 2 nm, comprising 100–400 atoms. We also optimize larger models (up to 3 nm length scale; ~3000 atoms) generated by other methods (see below) to compute their energy and structural characteristics.

Models at length scales above 6 nm and up to 20 nm are created *via* Monte-Carlo (MC) and Molecular Dynamics (MD) simulations using an empirical potential (Tersoff). While the empirical potential lacks the accuracy of DFT calculations and may not describe all configurations with equal fidelity, it allows the significant modeling of larger systems and gaining of valuable insight.

To bridge the gap between accurate DFT calculations and empirical potential simulations we have recently developed a new reactive force-field (ReaxFF).[73] Parameters for the reactive force-field have been carefully fitted to thermodynamic data including a library of DFT data of amorphous SiOC(:H) structures and properties. The new ReaxFF parameter set shows correspondence between ReaxFF and DFT simulations at small length scales. With its significantly lower computational demand in comparison to the electronic structure method, however, ReaxFF simulations can extend to larger length scales ultimately meeting the empirical potential simulations. The three atomistic simulation techniques together provide a multi-scale approach that corroborates the experimental data.

DFT calculations

The simulations within density functional theory[77] use the Vienna Ab Initio Simulation (VASP) package.[78,79] We use the Projector Augmented Wave (PAW) method[80,81] and approximate electron exchange and correlation by the Perdew–Burke–Ernzerhof (PBE) generalized gradient approximation (GGA). All simulations include a van der Waals correction.[82] We sample the Brillouin zone at the Γ-point.

We generate amorphous models of SiOC *via ab initio* molecular dynamics (aiMD) simulations with a "melt-quench" approach (aiMD-mq). Efficient model generation uses a "softer" version of carbon and oxygen pseudopotential, a time-step Δt = 1.0 fs, and a cutoff of 283 eV at this stage. The temperature of the system is adjusted by velocity scaling, and the volume is kept constant. We start the aiMD-mq simulation at 5000 K and use cooling rates of 12.5 to 100 K ps^{-1} until we reach T = 1500 K. Below 1500 K we use a cooling rate of 100 K ps^{-1} throughout. The last configuration of the trajectory (at 0 K) is optimized using "standard" pseudopotentials and a cutoff of 500 eV for the expansion of the wave function into the plane-wave basis set. Atomic positions and cell parameters relax to adjust to a local energy minimum state. Forces are converged to 5×10^{-2} eV $Å^{-1}$ and stresses to lower than 2 kbar.

Annealing of DHBP0.1_SG started with a model shown in Fig. 9b. We then heated the system in steps of 400 K to 3000 K, holding the system for 10 ps at every step. At 3000 K we let the system evolve for another 100 ps.

Empirical calculations

For empirical potential simulations of SiOC we use the Tersoff potential.[83–85] The hetero-atomic interaction parameters χ_{ij} and ω_{ij} are used to modify attractive interactions C–Si and C–O. Since neither DFT nor ReaxFF simulations yield meaningful fractions of C–O bonds, we use only repulsive interactions between C and O (ω_{C-O} = 0). General features of models – appearance of layered graphene and tubular, clustered carbon structures – are independent of whether attractive Si–C interactions are included not. Setting ω_{C-Si} = 0 only enhances clarity and is used for simulations shown in Fig. 10 and 11. All

structure simulations are performed using a Monte-Carlo method, introducing a random-walk between configurations. A new configuration is generated by displacing an atom (chosen at random) and its energy is computed. To decide whether a new configuration is accepted or not the energy difference ΔE between old and new configuration enters the Boltzmann factor $\exp(\Delta E/k_B{\cdot}T_{MC})$, ($k_B$ is the Boltzmann constant, T_{MC} is the Monte-Carlo temperature) which is then compared to a random number. In a model comprising N atoms, N such successful configuration changes are equal one (1) Monte-Carlo sweep (MCS). The distance for displacing atoms is adjusted at intervals to have a "success rate" of 10–20% for individual moves, but is limited between 0.1 and 50 pm. Starting with T_{MC} = 0, we increase T_{MC} to a maximum value within 5×10^4 MCS. We remain at the maximum T_{MC} for 1×10^5 MCS, and gradually decrease T_{MC} thereafter until it reaches zero. Choosing maximum values of T_{MC} of 0.3, 0.4, 0.5, and 0.6 the typical total length of a simulation is about 1.6×10^6 MCS. Structures depend somewhat on the length of annealing, but differences in final structures don't appear significant. Hence, the key parameter for developing a structure is the maximum value of T_{MC}.

ReaxFF modeling

For molecular dynamics (MD) simulations within ReaxFF we use LAMMPS software[86] and reax/c user's package.[87] We used a Bussi–Donadio–Parrinello thermostat[88] for temperature control. Time steps in our simulations vary from 0.1 fs to 1.0 fs depending on the hydrogen content of the simulated system. Parameters for the ReaxFF simulations have recently been published.[73] Melt-quench simulations of structures follow a standard approach, similar to the aiMD-MQ modeling described above. With ReaxFF we use cooling rates between 1 K ps^{-1} and 100 K ps^{-1}. Annealing a polymer follows a different approach. The time-temperature profile for polymer-to-ceramic simulations is shown in Fig. 14.

We first heat models of composition $SiC_{12}O_3H_8$ comprising 12 288 atoms to 3000 K to initiate reactions. Subsequently we anneal systems at 2000 K for 200 ps, followed by heating at 2500 and 300 K for 100 and 200 ps, respectively, before cooling them to 0 K. Every 25 ps in the course of simulations, we remove persistent gas molecules (H_2, CO, CO_2, H_2O, O_2, CH_2O, C_2H_2, C_2H_4) from the system.

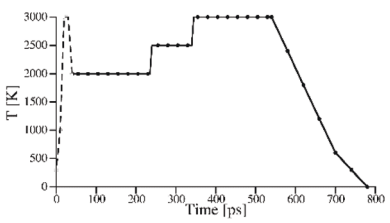

Fig. 14 Time *vs.* temperature scheme of annealing the polymer (Fig. 2) model of composition $SiC_{12}O_3H_8$ comprising 12 288 atoms. Dashed line – NVT ensemble, time step 0.1 fs; solid line – NPT ensemble, time step 0.2 fs. At the moments of time marked with points we removed gaseous molecules H_2, CO, CO_2, H_2O, O_2, CH_2O, C_2H_2, and C_2H_4.

Conflicts of interest

There are no conflicts to declare.

Acknowledgements

We gratefully acknowledge Prof. Ralf Riedel for the continuous support and valuable discussions. GM acknowledges the financial support from DFG (*Eigene Stelle* grant IO 83/2-1) and thanks Marco Melzi D'Eril for the FTIR and Raman spectroscopy technical support. PK acknowledges support by the National Science Foundation (NSF) through award CMMI-1634448. The computational work was made possible through generous grants by the Texas Advance Computing Center (TACC) in Austin, TACC, Texas, and by the High-Performance Computing facilities at UTA. The calorimetric measurements were performed at the University of California Davis supported by the A.P. Sloan Foundation Deep Carbon Observatory. EI acknowledges financial support from DFG (project "Micro-patterned polymer-derived ceramic catalysts and sensors" and the grant IO 64/14-1 within the Heisenberg program).

References

1 M. Narisawa, F. Funabiki, A. Iwase, F. Wakai and H. Hosono, *J. Am. Ceram. Soc.*, 2015, **98**, 3373–3380.
2 S. Iijima, *Nature*, 1991, **354**, 56.
3 X. Wang, W. Hu, Y. Liu, C. Long, Y. Xu, S. Zhou, D. Zhu and L. Dai, *Carbon*, 2001, **39**, 1533–1536.
4 M. Nath, B. C. Satishkumar, A. Govindaraj, C. P. Vinod and C. N. R. Rao, *Chem. Phys. Lett.*, 2000, **322**, 333–340.
5 M. Terrones, H. Terrones, N. Grobert, W. K. Hsu, Y. Q. Zhu, J. P. Hare, H. W. Kroto, D. R. M. Walton, P. Kohler-Redlich, M. Rühle, J. P. Zhang and A. K. Cheetham, *Appl. Phys. Lett.*, 1999, **75**, 3932–3934.
6 Y. Saito and T. Yoshikawa, *J. Cryst. Growth*, 1993, **134**, 154–156.
7 M. Terrones, A. Jorio, M. Endo, A. M. Rao, Y. A. Kim, T. Hayashi, H. Terrones, J. C. Charlier, G. Dresselhaus and M. S. Dresselhaus, *Mater. Today*, 2004, **7**, 30–45.
8 Z. R. Jia, K. C. Kou, M. Qin, H. J. Wu, F. Puleo and L. F. Liotta, *Catalysts*, 2017, **7**, DOI: 10.3390/catal7090256.
9 M. Lin, J. P. Y. Tan, C. Boothroyd, K. P. Loh, E. S. Tok and Y. L. Foo, *Nano Lett.*, 2007, **7**, 2234–2238.
10 R. T. K. Baker, *Bull. Am. Phys. Soc.*, 1981, **26**, 200–200.
11 T. Baker, *Chem. Ind.*, 1982, 698–702.
12 H. Yoshida, S. Takeda, T. Uchiyama, H. Kohno and Y. Homma, *Nano Lett.*, 2008, **8**, 2082–2086.
13 S. Costa, E. Borowiak-Palen, A. Bachmatiuk, M. H. Rummeli, T. Gemming and R. J. Kalenezuk, *Phys. Status Solidi B*, 2007, **244**, 4315–4318.
14 A. Bachmatiuk, E. Borowiak-Palen, M. H. Rummeli, T. Gemming and R. J. Kallenczuk, *Phys. Status Solidi B*, 2007, **244**, 3925–3929.

15 M. Audier, A. Oberlin, M. Oberlin, M. Coulon and L. Bonnetain, *Carbon*, 1981, **19**, 217–224.
16 O. C. Carneiro, M. S. Kim, J. B. Yim, N. M. Rodriguez and R. T. K. Baker, *J. Phys. Chem. B*, 2003, **107**, 4237–4244.
17 M. H. Rummeli, F. Schaffel, A. Bachmatiuk, D. Adebimpe, G. Trotter, F. Borrnert, A. Scott, E. Coric, M. Sparing, B. Rellinghaus, P. G. McCormick, G. Cuniberti, M. Knupfer, L. Schultz and B. Buchner, *ACS Nano*, 2010, **4**, 1146–1152.
18 P. T. A. Reilly and W. B. Whitten, *Carbon*, 2006, **44**, 1653–1660.
19 M. H. Rummeli, A. Bachmatiuk, F. Borrnert, F. Schaffel, I. Ibrahim, K. Cendrowski, G. Simha-Martynkova, D. Placha, E. Borowiak-Palen, G. Cuniberti and B. Buchner, *Nanoscale Res. Lett.*, 2011, **6**, DOI: 10.1186/1556-276X-6-303.
20 M. Kusunoki, M. Rokkaku and T. Suzuki, *Appl. Phys. Lett.*, 1997, **71**, 2620–2622.
21 D. Takagi, H. Hibino, S. Suzuki, Y. Kobayashi and Y. Homma, *Nano Lett.*, 2007, **7**, 2272–2275.
22 M. H. Rummeli, E. Borowiak-Palen, T. Gemming, T. Pichler, M. Knupfer, M. Kalbac, L. Dunsch, O. Jost, S. R. P. Silva, W. Pompe and B. Buchner, *Nano Lett.*, 2005, **5**, 1209–1215.
23 H. Liu, D. Takagi, H. Ohno, S. Chiashi, T. Chokan and Y. Homma, *Appl. Phys. Express*, 2008, **1**, 014001.
24 S. A. Steiner, T. F. Baumann, B. C. Bayer, R. Blume, M. A. Worsley, W. J. MoberlyChan, E. L. Shaw, R. Schlogl, A. J. Hart, S. Hofmann and B. L. Wardle, *J. Am. Chem. Soc.*, 2009, **131**, 12144–12154.
25 M. Bystrzejewski, A. Bachmatiuk, J. Thomas, P. Ayala, J. Serwatowski, H. W. Hubers, T. Gemming, E. Borowiak-Palen, T. Pichler, R. J. Kalenczuk, B. Buchner and M. H. Rummeli, *Phys. Status Solidi RRL*, 2009, **3**(6), 193–195.
26 A. Bachmatiuk, M. Bystrzejewski, F. Schaffel, P. Ayala, U. Wolff, C. Mickel, T. Gemming, T. Pichler, E. Borowiak-Palen, R. Klingeler, H. W. Hubers, M. Ulbrich, M. Knupfer, D. Haberer, B. Buchner and M. H. Rummeli, *Phys. Status Solidi B*, 2009, **246**, 2486–2489.
27 B. L. Liu, W. C. Ren, L. B. Gao, S. S. Li, S. F. Pei, C. Liu, C. B. Jiang and H. M. Cheng, *J. Am. Chem. Soc.*, 2009, **131**(6), 2082–2083.
28 S. M. Huang, Q. R. Cai, J. Y. Chen, Y. Qian and L. J. Zhang, *J. Am. Chem. Soc.*, 2009, **131**(6), 2094–2095.
29 A. Bachmatiuk, F. Borrnert, M. Grobosch, F. Schaffel, U. Wolff, A. Scott, M. Zaka, J. H. Warner, R. Klingeler, M. Knupfer, B. Buchner and M. H. Rummeli, *ACS Nano*, 2009, **3**, 4098–4104.
30 A. Bachmatiuk, F. Borrnert, F. Schaffel, M. Zaka, G. S. Martynkowa, D. Placha, R. Schonfelder, P. M. F. J. Costa, N. Ioannides, J. H. Warner, R. Klingeler, B. Buchner and M. H. Rummeli, *Carbon*, 2010, **48**, 3175–3181.
31 J. J. Schneider, N. I. Maksimova, J. Engstler, R. Joshi, R. Schierholz and R. Feile, *Inorg. Chim. Acta*, 2008, **361**, 1770–1778.
32 M. H. Rummeli, C. Kramberger, A. Gruneis, P. Ayala, T. Gemming, B. Buchner and T. Pichler, *Chem. Mater.*, 2007, **19**, 4105–4107.
33 L.-L. Tan, W.-J. Ong, S.-P. Chai and A. R. Mohamed, *Catal. Today*, 2013, **217**, 1–12.
34 H. P. Liu, D. Takagi, S. Chiashi and Y. Homma, *Carbon*, 2010, **48**, 114–122.
35 A. Hirsch, *Angew. Chem., Int. Ed.*, 2009, **48**, 5403–5404.
36 R. Riedel, G. Mera, R. Hauser and A. Klonczynski, *J. Ceram. Soc. Jpn.*, 2006, **114**, 425–444.
37 P. Colombo, G. Mera, R. Riedel and G. D. Soraru, *J. Am. Ceram. Soc.*, 2010, **93**, 1805–1837.
38 G. Mera, A. Navrotsky, S. Sen, H.-J. Kleebe and R. Riedel, *J. Mater. Chem. A*, 2013, **1**, 3826–3836.
39 C. Stabler, E. Ionescu, M. Graczyk-Zajac, I. Gonzalo-Juan and R. Riedel, *J. Am. Ceram. Soc.*, 2018, **101**, 4817–4856.
40 G. Mera, M. Gallei, S. Bernard and E. Ionescu, *Nanomaterials*, 2015, **5**, 468–540.
41 S. Widgeon, G. Mera, Y. Gao, E. Stoyanov, S. Sen, A. Navrotsky and R. Riedel, *Chem. Mater.*, 2012, **24**, 1181–1191.
42 A. H. Tavakoli, M. M. Armentrout, M. Narisawa, S. Sen and A. Navrotsky, *J. Am. Ceram. Soc.*, 2015, **98**, 242–246.
43 M. Graczyk-Zajac, D. Vrankovic, P. Waleska, C. Hess, P. V. Sasikumar, S. Lauterbach, H. J. Kleebe and G. D. Soraru, *J. Mater. Chem. A*, 2018, **6**, 93–103.
44 H. J. Kleebe, C. Turquat and G. D. Soraru, *J. Am. Ceram. Soc.*, 2001, **84**, 1073–1080.
45 C. Turquat, H.-J. Kleebe, G. Gregori, S. Walter and G. D. Sorarù, *J. Am. Ceram. Soc.*, 2001, **84**, 2189–2196.
46 D. Tománek, *Guide Through the Nanocarbon Jungle*, Morgan & Claypool Publishers, Williston, USA, 2014.
47 J. Gerard Lavin, S. Subramoney, R. S. Ruoff, S. Berber and D. Tománek, *Carbon*, 2002, **40**, 1123–1130.
48 J. Liu, L. Xu, W. Zhang, W. J. Lin, X. Chen, Z. Wang and Y. Qian, *J. Phys. Chem. B*, 2004, **108**, 20090–20094.
49 L. Zhang, X. Zeng and X. Wang, *Sci. Rep.*, 2013, **3**, 3162.
50 P. C. Eklund, J. M. Holden and R. A. Jishi, *Carbon*, 1995, **33**, 959–972.
51 D. E. H. Jones, *Nature*, 1996, **381**, 384–384.
52 C. Branca, F. Frusteri, V. Magazu and A. Mangione, *J. Phys. Chem. B*, 2004, **108**, 3469–3473.
53 J. L. Bantignies, J. L. Sauvajol, A. Rahmani and E. Flahaut, *Phys. Rev. B*, 2006, **74**(19), 195425-1–195425-5.
54 A. Misra, P. K. Tyagi, P. Rai and D. S. Misra, *J. Nanosci. Nanotechnol.*, 2007, **7**, 1820–1823.
55 R. Podila, R. Rao, R. Tsuchikawa, M. Ishigami and A. M. Rao, *ACS Nano*, 2012, **6**, 5784–5790.
56 S. Santangelo, G. Messina, G. Faggio, M. Lanza and C. Milone, *J. Raman Spectrosc.*, 2011, **42**, 593–602.
57 L. G. Cançado, K. Takai, T. Enoki, M. Endo, Y. A. Kim, H. Mizusaki, A. Jorio, L. N. Coelho, R. Magalhães-Paniago and M. A. Pimenta, *Appl. Phys. Lett.*, 2006, **88**, 163106.
58 L. G. Cançado, A. Jorio, E. H. M. Ferreira, F. Stavale, C. A. Achete, R. B. Capaz, M. V. O. Moutinho, A. Lombardo,

T. S. Kulmala and A. C. Ferrari, *Nano Lett.*, 2011, **11**, 3190–3196.
59 N. Larouche and B. L. Stansfield, *Carbon*, 2010, **48**, 620–629.
60 F. Rosenburg, PhD Thesis, Technische Universität Darmstadt, 2018.
61 E. V. Suslova, S. V. Savilov, J. Ni, V. V. Lunin and S. M. Aldoshin, *Phys. Chem. Chem. Phys.*, 2017, **19**, 2269–2275.
62 N. B. Cherkasov, S. V. Savilov, A. S. Ivanov and V. V. Lunin, *Carbon*, 2013, **63**, 324–329.
63 T. Varga, A. Navrotsky, J. L. Moats, R. M. Morcos, F. Poli, K. Müller, A. Saha and R. Raj, *J. Am. Ceram. Soc.*, 2007, **90**, 3213–3219.
64 A. H. Tavakoli, M. M. Armentrout, S. Sen and A. Navrotsky, *J. Mater. Res.*, 2015, **30**, 295–303.
65 J. Chen, S. W. King, E. Muthuswamy, A. Koryttseva, D. Wu and A. Navrotsky, *J. Am. Ceram. Soc.*, 2016, **99**, 2752–2759.
66 A. A. Levchenko, A. I. Kolesnikov, O. Trofymluk and A. Navrotsky, *Carbon*, 2011, **49**, 949–954.
67 B. S. Hemingway, J. L. Haas Jr. and G. R. Robinson Jr., *Thermodynamic properties of selected minerals in the system Al2O3-CaO-SiO2-H2O at 298.15 K and 1 bar (105 Pascals) pressure and at higher temperatures, Report 1544*, 1982.
68 L. Peng, W. Qisui, L. Xi and Z. Chaocan, *J. Therm. Anal. Calorim.*, 2009, **95**, 667–670.
69 D. H. Kuo and M. Y. Su, *Surf. Coat. Technol.*, 2007, **201**, 9172–9178.
70 H. Omachi, T. Nakayama, E. Takahashi, Y. Segawa and K. Itami, *Nat. Chem.*, 2013, **5**, 572–576.
71 A. Saha, R. Raj and D. L. Williamson, *J. Am. Ceram. Soc.*, 2006, **89**, 2188–2195.
72 A. C. T. van Duin, S. Dasgupta, F. Lorant and W. A. Goddard, *J. Phys. Chem. A*, 2001, **105**, 9396–9409.
73 I. Ponomarev, A. C. T. van Duin and P. Kroll, *J. Phys. Chem. C*, 2019, DOI: 10.1021/acs.jpcc.9b03810.
74 A. Navrotsky, *J. Am. Ceram. Soc.*, 2014, **97**, 3349–3359.
75 A. Navrotsky, *Phys. Chem. Miner.*, 1977, **2**, 89–104.
76 A. Navrotsky, *Phys. Chem. Miner.*, 1997, **24**, 222–241.
77 P. Hohenberg and W. Kohn, *Phys. Rev. B*, 1964, **136**, B864–B871.
78 G. Kresse and J. Hafner, *Phys. Rev. B: Condens. Matter Mater. Phys.*, 1994, **49**, 14251–14269.
79 G. Kresse and J. Furthmuller, *Phys. Rev. B: Condens. Matter Mater. Phys.*, 1996, **54**, 11169–11186.
80 P. E. Blochl, *Phys. Rev. B: Condens. Matter Mater. Phys.*, 1994, **50**, 17953–17979.
81 G. Kresse and D. Joubert, *Phys. Rev. B: Condens. Matter Mater. Phys.*, 1999, **59**, 1758–1775.
82 S. Grimme, *J. Comput. Chem.*, 2006, **27**, 1787–1799.
83 J. Tersoff, *Phys. Rev. B: Condens. Matter Mater. Phys.*, 1988, **38**, 9902–9905.
84 J. Tersoff, *Phys. Rev. Lett.*, 1988, **61**, 2879–2882.
85 Y. Umeno, T. Kitamura, K. Date, M. Hayashi and T. Iwasaki, *Comput. Mater. Sci.*, 2002, **25**, 447–456.
86 S. Plimpton, *J. Comput. Phys.*, 1995, **117**, 1–19.
87 H. M. Aktulga, J. C. Fogarty, S. A. Pandit and A. Y. Grama, *Parallel Comput.*, 2012, **38**, 245–259.
88 G. Bussi, D. Donadio and M. Parrinello, *J. Chem. Phys.*, 2007, **126**, 014101-1–014101-7.

